

CFD analysis of the influence of solvent viscosity ratio on the creeping flow of viscoelastic fluid over a channel-confined circular cylinder

Pratyush Kumar Mohanty^{a,*}, Akhilesh Kumar Sahu^{a,**}, Ram Prakash Bharti^{b,**}

^aComputational Flow Modelling (CFM) Research Lab, Department of Chemical Engineering, National Institute of Technology, Rourkela 769008, Odisha, India

^bComplex Fluid Dynamics and Microfluidics (CFDM) Lab, Department of Chemical Engineering, Indian Institute of Technology Roorkee, Roorkee 247667, Uttarakhand, India

Abstract

In this study, the role of solvent viscosity ratio (β) on the creeping flow characteristics of Oldroyd-B fluid over a channel-confined circular cylinder has been explored numerically. The hydrodynamic model equations have been solved by RheoTool, an open-source toolbox based on OpenFOAM, employing the finite volume method for extensive ranges of Deborah number ($De = 0.025 - 1.5$) and solvent viscosity ratio ($\beta = 0.1 - 0.9$) for the fixed wall blockage ($B = 0.5$). The present investigation has undergone extensive validation, with available literature under specific limited conditions, before obtaining detailed results for the relevant flow phenomena such as streamline, pressure and stress contour profiles, pressure coefficient (C_p), wall shear stress (τ_w), normal stress (τ_{xx}), first normal stress difference (N_1), and drag coefficient (C_D). The flow profiles have exhibited a distinctive behavior characterized by a loss of symmetry in the presence of pronounced viscoelastic and polymeric effects. The results for low De notably align closely with those for Newtonian fluids, and the drag coefficient (C_D) remains relatively constant regardless of β , as the viscoelastic influence is somewhat subdued. As De increases, the influence of viscoelasticity becomes more pronounced, while a decrease in β leads to an escalation in polymeric effects; an increase in the C_D value is observed as β increases. Within this parameter range, the prevailing force governing the flow is the pressure drag force.

Keywords: Creeping flow, Viscoelastic fluid, Viscosity ratio, Polymeric effect, Drag coefficient, Non-Newtonian fluid

1. Introduction

The flow over a cylinder is represented as a conventional bluff body dynamics problem because of its essential nature and vast applicability [1, 2]. Despite a simple geometry, this forms the basis for understanding the underlying physics behind flow past complex geometries. It has several industrial uses, such as cooling towers, nuclear reactors, chimney stacks, heat exchangers of the pin and tube types, flow control, and drag reduction techniques. A significant knowledge framework has been established using analytical, experimental, and computational approaches over the years, and numerous studies have explored multiple facets of fluid flow past circular cylinders in static and rotating conditions for both Newtonian and non-Newtonian fluids [3–11].

Intricate non-Newtonian characteristics, such as yield stress, shear-rate dependence of viscosity, and viscoelasticity, are commonly recognized in fluids that contain high molecular weight polymers [12, 13]. Viscoelastic fluids possess the ability to both store and release energy over time, as they exhibit both viscous and elastic behaviour. In industrial operations, the properties of such fluids can substantially affect momentum transfer. Due to the complexity and difficulties in anticipating the viscoelastic fluid behaviour, plenty of viscoelastic fluid phenomena still need to be discovered.

Researchers have employed various experimental and computational methods to comprehend the detailed behavior of viscoelastic fluids and their effect on momentum transfer. Understanding the effects of shear rate, pressure, and temperature on fluid behaviour and devising models that can accurately predict the behaviour of these fluids in industrial contexts are among the areas of emphasis [14, 15]. Despite the challenges associated with studying viscoelastic fluids, there have been significant advances in the past several years. Some widely used viscoelastic models are Kelvin, Maxwell, FENE-P, Oldroyd-B. Our investigation uses the

*Undergraduate student (Research intern, CFDM Lab, Chemical Engineering, IIT Roorkee; December 2022)

**Corresponding author

Email addresses: sahuak@nitrrkl.ac.in (A.K. Sahu), rpbharti@iitr.ac.in (R.P. Bharti)

Oldroyd-B constitutive model, which accurately captures the rheological behavior of the viscoelastic fluids. The adoption of this model is justified due to its simplicity, based on a sole conformation tensor and two parameters related to relaxation time and polymer concentration [16]. There is a voluminous literature on the fluid flow behaviour of an Oldroyd-B fluid over a circular cylinder at a constant solvent viscosity ratio (β). However, none of the studies depicts the role of solvent viscosity ratio (β) on the fluid flow characteristics over a confined cylinder. Therefore, the purpose of this research is to address the existing gap in the literature. Nevertheless, a concise overview of the existing knowledge on Newtonian and non-Newtonian fluids flow over a cylinder is presented to conceptualize the significance of the present study.

2. Literature Review

Over the century, the flow over a cylinder has been one of the most classically researched problems to understand the hydrodynamics of bluff bodies, as evidenced by several excellent articles and books [3–11, 17, 18] featuring the varieties of the flow characteristics of both Newtonian (and non-Newtonian) fluids around unconfined (and channel-confined) cylinders. Numerous outstanding studies have demonstrated the influence of wall blockage on the fluid flow characteristics of a cylinder using different means of analysis [10, 11]. In this section, the literature focusing on Newtonian and non-Newtonian fluid flow around a confined circular cylinder has been reviewed, followed by the detailed literature analysis for Oldroyd-B fluid flow past the cylinder.

Zdravkovich [5, 6] comprehended the existing knowledge to present the fundamental aspect of the Newtonian flow over a cylinder, including the detailed characterization of flow regimes and highlighted the crucial flow kinematics such as flow transition and wake separation. Zovatto and Pedrizzetti [19] conducted in-depth numerical analysis on the impact of wall confinement on two-dimensional steady to vortex shedding flow of Newtonian fluid over a cylinder using the vorticity-stream function formulation and finite element method. In a numerical analysis of the steady laminar flow ($Re = 0.1 - 200$) of a Newtonian fluid around a circular cylinder

situated within a planar rectangular channel (blockage ratio, $B = H/D = 1.54 - 20$), Chakraborty et al. [20] reported a reduction in drag coefficient (C_D) with increasing B (for fixed Re) and increasing Re (for fixed B). Further, both separation angle and wake length increased with increasing Re (for fixed B). Mettu et al. [21] numerically evaluated the forced convection from an isothermal cylinder confined asymmetrically (gap ratio, $G = 0.125 - 1$; $G = 1$ for symmetric) in a planar channel for $Re = 10 - 500$, $Pr = 0.744$, $B = 2.5 - 10$. They observed an increase in critical Re for transiting steady to unsteady flow, an increase in both drag (C_D) and Strouhal number (St), and a negligible influence on Nusselt number (Nu) with decreasing G for all values of B . For low Re flow over a confined cylinder, Singha and Sinhamahapatra [22] confirmed delayed transition in the vortex shedding with decreasing B due to the strengthening interaction between wake and channel walls and stated that St exhibited independence from Re for low B . Sahin and Owens [23] performed linear stability analysis to assess the stability of the steady asymmetric solutions for the Newtonian flow ($0 < Re < 280$) around a channel-confined ($0.1 < B < 0.9$) cylinder. They observed that the asymmetric flows become unstable as well, transitioning to unsteadiness through a Hopf bifurcation for $B > 0.82$. Subsequently, Mishra et al. [24] outlined that the presence of large confinement ($B = 0.9$) stabilizes the 2-D flow ($Re = 4 - 100$) over a cylinder. The confinement delays the start of laminar separation until $Re = 27.8$. Additionally, the steady-state flow was maintained up to $Re = 100$. They also observed that the sudden decrease in surface pressure around the cylinder and the delayed appearance of an abrupt pressure gradient across the cylinder surface are direct outcomes of substantial blockage.

Further, existing literature has significantly explored the flow of power-law fluids around both circular and non-circular cylinders. For instance, the drag and heat transfer characteristics are reported to be complex [25, 26] for the steady power-law flow ($1 \leq Re \leq 40$, $0.2 \leq n \leq 1.9$, $1 \leq Pr \leq 100$) across the channel-confined ($1.1 \leq B \leq 4$) cylinder. Similarly, unsteady power-law fluid flow around a confined circular cylinder has been investigated under a broad range of parameters $0.4 < n < 1.8$, $40 < Re < 140$, $B = 2, 4$, and 6 [27] and for $0.4 < n < 1.8$,

$50 < Re < 150$, $B = 4$ [28, 29]. Vishal et al. [30] determined the critical parameters for shear-thickening ($1 < n < 1.8$) power-law fluid flow through a channel-confined circular cylinder for two wall blockage ratio values ($B = 2$ and 4) using open-source finite volume solver OpenFOAM, and supplemented the results for the critical parameters for unconfined ($B = \infty$) power-law fluid flow [31] obtained using commercial finite volume solver Ansys FLUENT.

In contrast, the studies related to the Oldroyd-B fluid flowing over a confined cylinder are scant compared to its Newtonian and power-law counterparts. Most of the investigations have considered a constant solvent viscosity ratio ($\beta = 0.59$, i.e., Boger fluid) for a fixed blockage ratio ($B = 2$) and Deborah number ranging from 0 to 2 [32–36]. Oliveira et al. [37] developed a new finite volume methodology for the computation of the viscoelastic fluid flow. The proposed approach for acquiring stress values at cell faces was demonstrated effectively, as it successfully eradicates oscillations in the calculated profiles for various quantities even at high De . This technique has subsequently been improved [38] for the Oldroyd-B and upper convected Maxwell (UCM) fluids by employing two high-resolution methods, namely, SMART and MINMOD. The numerical accuracy of the improved technique was ascertained in the literature [32–34] by comparing the drag and lift coefficient (C_D and C_L) values for the benchmark channel confined ($B = 0.5$) cylinder flow problem. Dou and Phan-Thien [39] adopted the Oldroyd-B model to compute the confined flow around a circular cylinder. They observed decreasing drag coefficient at low De (≤ 0.6); however, it increases for higher De as De increases. Additionally, they demonstrated that the pressure distortion near the cylinder originates from the interplay of normal stress and the influence of streamline curvature, inducing an inflection in the velocity profile. Consequently, induced flow distortion contributes to the overall instability of the flow field. Richter et al. [40] numerically illustrated the significant influence of dilute polymer additives on the three-dimensional inertial flow of viscoelastic (L2 in the FENE-P model) fluid past a cylinder at $Re = 100$ and 300 . Recently, Minaeian et al. [41, 42] have numerically analyzed viscoelastic effects on the onset of vortex

shedding over a channel confined ($B = 0.05$) circular cylinder for a high concentration polymer solution governed by the Phan–Thien–Tanner (PTT) model for wide range of elasticity number ($El = 0 - 100$) at $Re = 100$ using the rheoFoam - OpenFOAM solver based on the finite volume method. Hopkins et al. [43] reported novel inertia-less, shear-thinning viscoelastic flow instability for wormlike micellar solution flowing past a confined ($B = 0.5$) microcylinder for broad Weissenberg number ($0.5 \leq Wi \leq 900$). Kumar and Ardekani [44] have numerically explored the hysteresis in pulsatile viscoelastic (FENE-P model) flow instability of confined cylinders using RheoTool integrated with openFOAM and log-confirmation approach for polymeric stress tensor for small Reynolds number ($Re = 0.0004 - 0.004$), constant elasticity number ($El = 781.25$), and range of Weissenberg number ($0 \leq Wi \leq 4$).

Based on the above discussion of the existing relevant literature, it is notable that limited studies have focused on the viscoelastic (Oldroyd-B) fluid flowing past a confined circular cylinder. To the best of our knowledge, prior studies have not analyzed the impact of solvent viscosity ratio on the flow characteristics of viscoelastic fluid across a channel-confined circular cylinder. Therefore, current work aims to understand the role of the solvent viscosity ratio (β) and Deborah number (De) on the viscoelastic fluid flow characteristics across a confined circular cylinder in the creeping flow regime using finite volume method open-source solved RheoTool integrated with openFOAM and log-confirmation approach for polymeric stress tensor.

3. Problem Formulation

The current study examines the flow properties of a viscoelastic fluid in a two-dimensional (2-D) laminar creeping flow past a circular cylinder (diameter D), confined within the two parallel walls spaced apart by a distance H , as shown schematically in Fig. 1. The inlet flow is considered to have a fully developed velocity profile with a maximum velocity of U_{\max} and an average velocity of $U_{\text{avg}} = (2/3)U_{\max}$. In order to preclude any three-dimensional (3-D) effects, the cylinder is taken to be infinitely long along the z -axis. The wall blockage ratio (B) is defined

as $B = D/H$. The cylinder is horizontally positioned with center (x_c, y_c) at $(L_u, H/2)$, where L_u is the upstream length measured from the inlet to the center of the cylinder. The geometrical specifications (length and height) of the rectangular computational flow domain are $L(= L_u + L_d)$ and H , where L_d is the downstream length measure from the center of the cylinder to outlet. Further, $\theta = 0^\circ$ (or 360°) represents the rear stagnation point (RSP), and $\theta = 180^\circ$ indicates the front stagnation point (FSP) on the surface of the cylinder.

Oldroyd [45] marked the initial attempt to establish constitutive models for viscoelastic fluids while systematically upholding material frame indifference. According to this theory, stress in a continuous media should only be caused by deformations and should not be affected by simple rotation of the material. In this study, the rheological nature of the viscoelastic fluid is defined by the Oldroyd-B model because it adequately approximates a Boger fluid by having a quadratic first normal stress difference, constant shear viscosity, and zero second normal stress difference. The flow problem is mathematically governed by the continuity and momentum equations in

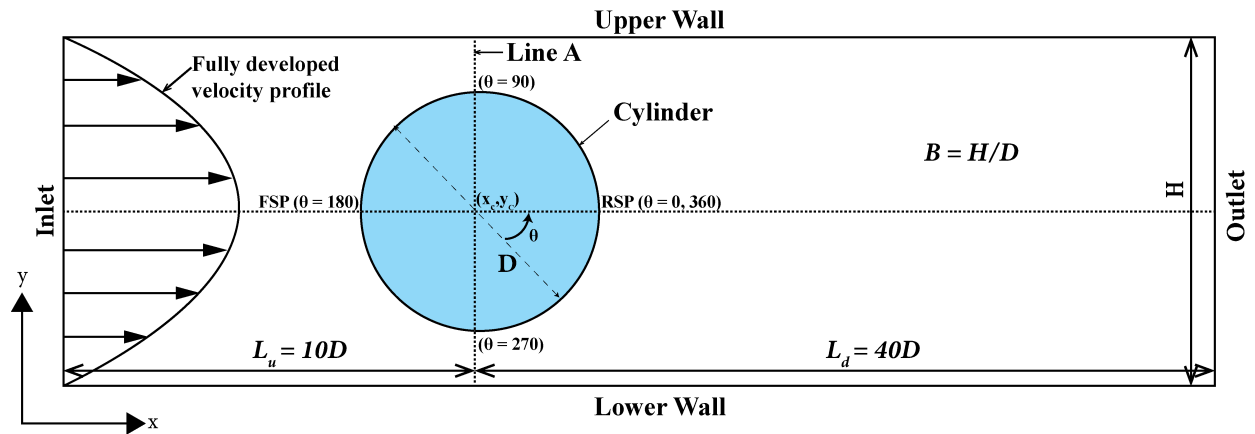


Figure 1: Schematic representation of the computational flow arrangement.

conjunction with the Oldroyd-B viscoelastic model as follows.

$$\frac{\partial u_x}{\partial x} + \frac{\partial u_y}{\partial y} = 0 \quad (\text{continuity equation}) \quad (1)$$

$$\rho \left[\frac{\partial u_x}{\partial t} + \frac{\partial(u_x u_x)}{\partial x} + \frac{\partial(u_x u_y)}{\partial y} \right] = -\frac{\partial p}{\partial x} + \left[\frac{\partial \tau_{xx}}{\partial x} + \frac{\partial \tau_{xy}}{\partial y} \right] \quad (\text{x-momentum equation}) \quad (2)$$

$$\rho \left[\frac{\partial u_y}{\partial t} + \frac{\partial(u_y u_x)}{\partial x} + \frac{\partial(u_y u_y)}{\partial y} \right] = -\frac{\partial p}{\partial y} + \left[\frac{\partial \tau_{yx}}{\partial x} + \frac{\partial \tau_{yy}}{\partial y} \right] \quad (\text{y-momentum equation}) \quad (3)$$

In the equations expressed above, u_x , and u_y represents the x - and y - components of velocity vector (\mathbf{U}), ρ is the density of the fluid, and p denotes pressure. The extra-stress tensor (τ) is a combination of stress due to solvent (τ_s) and stress due to polymer (τ_p) as follows.

$$\tau = \tau_s + \tau_p \quad (4)$$

The stress due to solvent is expressed as follows:

$$\tau_s = 2\eta_s \mathbf{D}, \quad \text{where} \quad \mathbf{D} = \frac{1}{2} [(\nabla \mathbf{U}) + (\nabla \mathbf{U})^T] \quad (5)$$

where, \mathbf{D} is the deformation rate tensor and η_s is the viscosity of the solvent.

The polymeric stress tensor (τ_p) is computed by the log-conformation method using the non-dimensional configuration tensor (\mathbf{A}), in accordance with the Oldroyd-B model as follows:

$$\tau_p = \frac{\eta_p}{\lambda} (\mathbf{A} - \mathbf{I}) \quad (6)$$

$$\overset{\nabla}{\mathbf{A}} = \frac{1}{\lambda} (\mathbf{A} - \mathbf{I}) \quad (7)$$

In the above equations, η_p is the polymeric viscosity, λ denotes the relaxation time, \mathbf{I} represents an identity tensor, and $\overset{\nabla}{\mathbf{A}}$ is Oldroyd derivative which is given by

$$\overset{\nabla}{\mathbf{A}} = \frac{\partial \mathbf{A}}{\partial t} + \mathbf{U} \cdot \nabla \mathbf{A} - (\nabla \mathbf{U})^T \cdot \mathbf{A} - \mathbf{A} \cdot (\nabla \mathbf{U}) \quad (8)$$

The boundary conditions for the current flow problem are written as follows:

- *At the inlet boundary:* Fluid enters the computational domain with a fully developed

velocity field at the inlet ($0 \leq y \leq H$). In addition, a pressure gradient and the excess stress tensor are ascribed to a value of zero. Mathematically, it is expressed as follows.

$$u_x = U_{\text{avg}} \left(1 - \left| 1 - \frac{2y}{H} \right|^2 \right), \quad u_y = 0, \quad \frac{\partial p}{\partial x} = 0 \quad \text{and} \quad \tau = 0 \quad (9)$$

- *On the cylinder surface, upper and lower walls:* The no-slip velocity condition is used, and the gradient of the pressure is taken to be zero, mathematically expressed as follows. Further, the extra stress tensor is calculated using linear extrapolation.

$$u_x = 0, \quad u_y = 0, \quad \text{and} \quad \frac{\partial p}{\partial n} = 0 \quad (10)$$

where, n refers to the direction normal to the boundary.

- *At the outlet boundary:* The gradient of velocity is assigned a zero value means there is no diffusion flux along the direction normal to the outlet and pressure is ambient.

$$\frac{\partial u_x}{\partial x} = 0, \quad \frac{\partial u_y}{\partial x} = 0 \quad \text{and} \quad p = 0 \quad (11)$$

In this work, the dimensionless groups governing the considered flow problem are defined as follows, based on the scaling of the velocity field, pressure field and the stress components with the average velocity (U_{avg}), dynamic pressure ($\frac{1}{2}\rho U_{\text{avg}}^2$) and dynamic stress ($\tau_0 = \eta_0 U_{\text{avg}}/D$), respectively.

- Solvent viscosity ratio (β) is expressed as follows.

$$\beta = \frac{\eta_s}{\eta_0} = \frac{\eta_s}{\eta_s + \eta_p} \quad (12)$$

where, η_0 is the total viscosity of the viscoelastic material.

- Reynolds number (Re) relating inertial to viscous force is given as follows.

$$Re = \frac{\rho U_{\text{avg}} D}{\eta_0} \quad (13)$$

- Deborah number (De) characterizing the fluidity of viscoelastic material relates the relaxation time of the material to the characteristic time scale as follows.

$$De = \frac{\lambda U_{\text{avg}}}{D} \quad (14)$$

where, λ is the relaxation time; it is the characteristic property of the material [46].

Furthermore, the flow characteristics and engineering parameters deduced from the numerically obtained flow fields are defined as follows. The total drag coefficient (C_D) over the surface of a cylinder [25] is evaluated using the following expression.

$$C_D = \frac{F_D}{\eta_0 U_{\text{avg}}} = \frac{1}{\eta_0 U_{\text{avg}}} \int_S (-p\mathbf{I} + \boldsymbol{\tau}) \cdot \hat{\mathbf{i}} \cdot d\mathbf{S} \quad (15)$$

where, F_D is the total drag force acting in the flow direction over the per unit length of the cylinder, \mathbf{S} is the surface area of the cylinder, \mathbf{I} is identity matrix and $\hat{\mathbf{i}}$ is a unit vector in the flow (i.e., x -) direction. The two additive terms in Eq. (15) indicating the contribution of pressure and viscous forces are commonly referred to as the pressure drag coefficient (C_{DP}) and viscous drag coefficient (C_{DF}), respectively.

The magnitude of the wall shear-stress (WSS) over the surface of the cylinder is obtained using

$$\tau_w = |\hat{\mathbf{n}} \cdot \boldsymbol{\tau} - \hat{\mathbf{n}}(\hat{\mathbf{n}} \cdot \boldsymbol{\tau} \cdot \hat{\mathbf{n}})| \quad (16)$$

where $\hat{\mathbf{n}}$ is the unit vector normal to the surface of cylinder.

The pressure coefficient (C_p) over the surface of the cylinder [25] is evaluated as.

$$C_p = \frac{(p - p_\infty)}{\frac{1}{2}\rho U_{\text{avg}}^2} \quad (17)$$

where, p_∞ is the pressure far away from the cylinder under the fully developed condition.

4. Numerical Methodology

In this study, an open-source toolbox, rheoTool v6 [47, 48], based on the finite volume method (FVM) CFD open-source code OpenFOAM v7 [49], is used to solve viscoelastic flow governing equations described in the previous section. The Oldroyd-B model has been used to govern the rheological nature of the viscoelastic fluid material. The high-resolution CUBISTA (Convergent and Universally Bounded Interpolation Scheme for Treatment of Advection) scheme has been used to discretize the advective components of the momentum and constitutive equations because of its superior convergence features [50]. The temporal derivative terms are discretized using the linear interpolation technique, and the diffusive terms in the momentum equation have been discretized using the Gauss linear interpolation scheme. An open-source mesh generator, Gmsh v4.11.1 [51], has been used to discretize the computational domain and generate a suitable computational grid structure. The mesh is then imported to OpenFOAM. The solution of linearized algebraic equations has been obtained by interfacing the rheoTool with the sparse matrix solvers of PETSc (Portable, Extensible Toolkit for Scientific Computation) (v 3.15) library [52, 53] that utilizes the direct preconditioner, PCLU, a direct solver for the linear system that employs LU factorization. The stress field is solved using the PBiCG (Preconditioned Bi-conjugate Gradient) solver along with DILU (Diagonal-based Incomplete LU) preconditioner [54, 55]. The SIMPLE (Semi-Implicit Method for Pressure Linked Equations) technique has been used to establish the pressure-velocity coupling and the numerical solution is stabilized using the log-conformation tensor method [47, 56]. The semi-coupled solver, wherein pressure and velocity are coupled, and stress is segregated, is used to obtain the fully converged solution (with a relative tolerance of 10^{-10}) for the pressure, velocity, and stress fields.

The appropriate selection of computational and numerical parameters (such as domain dimensions, grid resolution, and time-step size) is significant to the precision of the obtained results. It is, therefore, important to suitably select these parameters by trade-off the accuracy of results and the least amount of computing time. As outlined in the preceding section, the

computational domain is characterized by upstream length, L_u and downstream length, L_d . Based on the systematic domain independence study and our previous experience [25], the optimal values are selected as $L_u = 10D$ and $L_d = 30D$ for the fixed blockage ratio ($B = 0.5$) to alleviate the end effects considering the imposed fully developed inlet and outlet con

After selecting the appropriate computational domain ($L_u = 10D$, $L_d = 30D$, $B = 0.5$), an extensive grid independence study is performed to ensure the independence of numerical results on the grid structure resulting from the spatial discretization of the computational domain. Four distinct non-uniform unstructured grids G1 to G4 (shown schematically in Figure 2) generated using open-source mesh generator Gmsh v4.11.1 [51] are used to perform the grid independence study. Table 1 displays the mesh characteristics (N_c is the number of nodes on

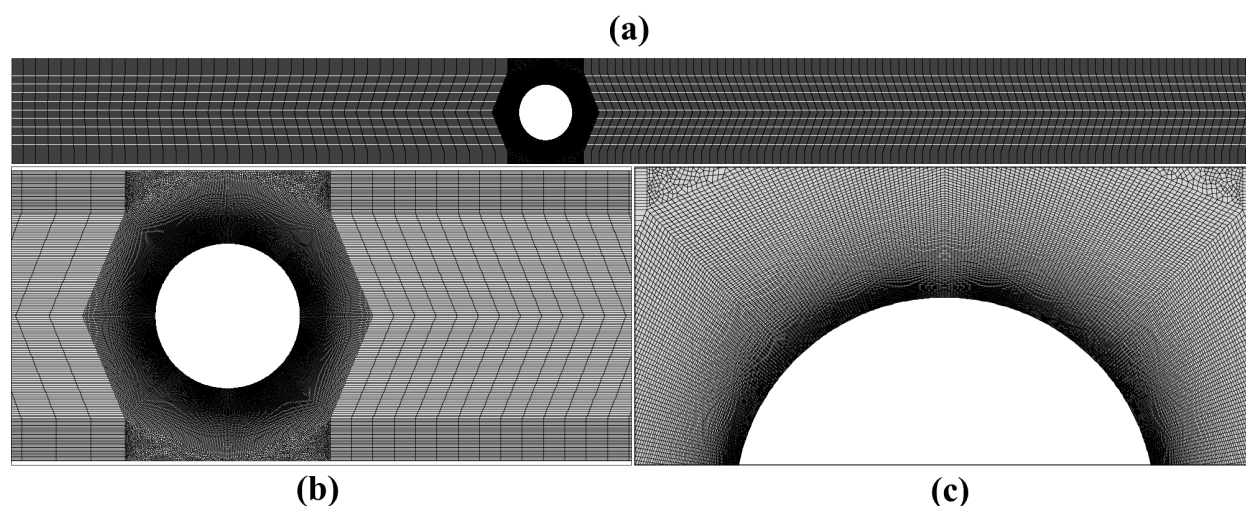


Figure 2: Schematics of mesh (a) in the whole computational domain (b) around the cylinder (c) zoomed view near the cylinder.

Table 1: Grid independence test for extreme values of Deborah number ($De = 0.025$ and 1.5) and solvent viscosity ratio ($\beta = 0.1$ and 0.9).

Grid	N_c	N_n	N_e	Drag Coefficient (C_D)			
				$De = 0.025, \beta = 0.1$	$De = 0.025, \beta = 0.9$	$De = 1.5, \beta = 0.1$	$De = 1.5, \beta = 0.9$
G1	240	129882	195493	131.0147	132.3322	115.5089	140.4210
G2	480	158202	237973	131.1744	132.6261	118.5783	143.2001
G3	720	186522	280453	131.2015	132.6828	118.3904	143.8222
G4	960	214842	322933	131.2128	132.7055	118.6864	143.9110

the surface of the cylinder, N_n is total number of nodes in the computational domain, and N_e is total number of quadrilateral mesh elements in the computational domain) and the influence of mesh on the drag coefficient (C_D) for extreme values of Deborah number ($De = 0.025$ and 1.5) and solvent viscosity ratio ($\beta = 0.1$ and 0.9). An analysis of Table 1 suggests that the C_D values show insignificant change ($< 1\%$) with refinement in the grid from G2 to G3 and G4. Therefore, considering the significant enhancement in the computation efforts with mesh refinement, grid G2 is selected to obtain the new results presented in this work. Furthermore, while the considered problem is time-independent, the time-step of $\Delta t = 0.001s$ is selected for the present study, as the openFOAM utilizes false-transient approach to obtain the numerical solution.

5. Results and discussion

The current investigation has explored the influences of the solvent viscosity ratio ($0.1 \leq \beta \leq 0.9$) and Deborah number ($0.025 \leq De \leq 1.5$) on the momentum transfer characteristics of a channel-confined ($B = 0.5$) cylinder submerged in low Reynolds number ($Re = 0.01$) creeping flow of viscoelastic fluid rheologically governed by the Oldroyd-B model. The novelty and significance of the considered parameters for investigation are as follows. For larger β , the fluid typically shows Newtonian behavior as very little to negligible polymeric components in the polymeric solution. As the value of β decreases, it tends to become more polymeric. For example, dilute polymer solutions in water have low β ($= 0.1 - 0.3$), concentrated polymer solutions or suspensions have moderate β ($= 0.4 - 0.6$), whereas hydrogels or suspensions with a high solid particle content have high β ($= 0.7 - 0.9$). Further, a broad range of Deborah numbers (De) covers the variety of viscoelastic fluids, from almost pure viscous fluids ($De = 0.025$) to highly viscoelastic fluids ($De = 1.5$). Such an investigation is essential for gaining insights into viscoelastic fluid flow in various scientific and engineering applications [57–59]. In this section, the modeling approach has first been validated to ensure the accuracy and reliability of the new results. Subsequently, the detailed results have been shown to

elaborate the influence of the flow governing parameters (β , De) on the flow characteristics (such as streamline, pressure, and the normal stress contour profiles, pressure coefficient, normal and wall shear stress over the cylinder, and velocity profiles, drag coefficient and its components).

5.1. Validation

In order to ensure the reliability and accuracy of the new result presented in this work, the numerical modeling approach has been validated by comparing the present results for the drag coefficient (C_D) with previously reported data [14, 38, 60–62] in Table 2. It is evident from the Table 2 that the present results are in good agreement ($< 1\%$) with the literature results, particularly within the low Deborah number range ($De < 1.2$). Further, no oscillations are observed even at high Deborah numbers ($De = 1.5$) in this study. This observation of the current analysis shows strong agreement with the literature [60] data, which reported no oscillations even up to $De = 1.8$. However, the present results do not align well with other literature values, as those studies exhibit oscillations at high Deborah numbers other studies [14, 38, 61, 62] exhibit oscillations at high De , possibly due to inadequate mesh refinement, due to which present and literature results are not as closely aligned as with [60]. Keeping note that the considered studies [14, 38, 60–62] have used different modeling and numerical approaches to obtain the numerical solution, the present results are considered to display excellent ($\pm 1\%$)

Table 2: Comparison of the present C_D values with literature for creeping ($Re \rightarrow 0$) flow.

De	Present study	Dou and Phan-Thien [60]	Fan et al. [61]	Liu et al. [14]	Sun et al. [62]	Alves et al. [38]
0.025	132.0944	131.5020	–	–	–	–
0.050	130.6353	131.0823	–	–	–	–
0.100	126.9604	129.7226	130.3597	–	130.3283	130.3069
0.300	126.9605	123.5148	123.1893	–	123.2597	123.1504
0.500	118.6448	120.5768	118.8301	119.5024	119.1053	118.8137
0.700	122.8196	121.1297	117.3196	118.5398	117.8361	117.3435
0.900	129.4620	124.4799	117.7996	–	118.5033	117.9064
1.100	137.9596	133.1570	–	–	120.3845	–
1.300	147.5921	136.9420	–	–	123.0674	–
1.500	157.8138	147.1723	–	–	126.3221	–

accuracy and reliable for design and engineering of relevant applications. This comparative analysis offers further confidence in the accuracy and reliability of the current modeling approach.

5.2. Streamline patterns

In this section, the detailed flow characteristics are presented and analyzed using the streamline (ψ) patterns (Fig. 3) for the extreme values of dimensionless parameters (β , De). Uniformly distributed ($\delta\psi = 0.2$) contour lines ranging from $\psi_{\min} = 0$ to $\psi_{\max} = 3$ are drawn in Fig. 3. As expected, no flow separation behind the cylinder is depicted in Fig. 3 over the range of conditions. Viscous force is the main factor causing the flow to be creeping. The viscous force makes the fluid adhere to the surface of the cylinder, thereby preventing any separation or

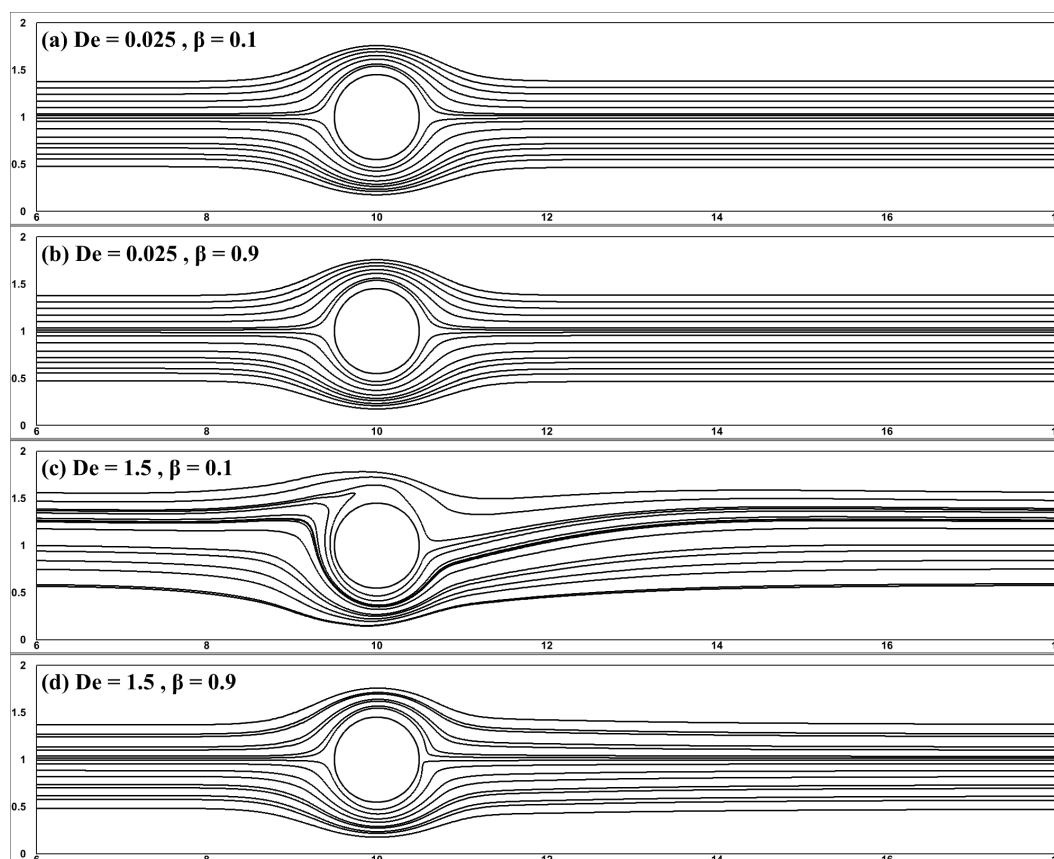


Figure 3: Streamline patterns around the cylinder at (a) $De = 0.025$, $\beta = 0.1$, (b) $De = 0.025$, $\beta = 0.9$, (c) $De = 1.5$, $\beta = 0.1$, (d) $De = 1.5$, $\beta = 0.9$.

detachment, and flow remains attached. At a low value of Deborah numbers ($De = 0.025$), the effect of β on the streamline patterns is not significant, as observed in Fig. 3(a, b). This phenomenon can be ascribed to the fact that when the Deborah number is low, the viscoelastic effect is diminished due to the shorter relaxation times, resulting in decreased polymeric effects. As a result, the solvent viscosity ratio (β) has minimal impact on the streamlines for low De . However, the streamline profiles at the higher Deborah number ($De = 1.5$) are seen to be asymmetric for lower β (≤ 0.2) and symmetric for β (> 0.2) about the horizontal centerline (x, y_c), as depicted in Fig. 3(c, d). At high Deborah numbers (De), the effects of elastic forces within the fluid become more pronounced. As the ratio of solvent viscosity (β) decreases, the flow behaviour is increasingly influenced by the elastic properties of the fluid, and the polymeric effects increases. This increased elastic effect due to major polymeric contribution has the potential to cause additional deformation and elongation of the fluid constituents or elements, thereby leading to evident adaptations in the streamline. Having observed the complex dependence of the streamline patterns on the Deborah number (De) and the solvent viscosity ratio (β), the subsequent section explores the pressure and stress profiles to gain further insights into the flow.

5.3. Pressure and stress patterns

Fig. 4 illustrates the scaled pressure (p) contours around the cylinder for the extreme values of the Deborah number (De) and the solvent viscosity ratio (β). Uniformly distributed ($\delta p = 200$) contour lines ranging from $p_{\min} = 2000$ to $p_{\max} = 22000$ are drawn in Fig. 4. The variation in dynamic pressure surrounding the cylinder is observed to increase by 30.43 % with increasing Deborah number (De) from 0.025 to 1.5. At the low value of De , the pressure contours are seen to be symmetric around the cylinder in Fig. 4(a, b). There is, however, a pronounced pressure gradient in the vicinity of the cylinder at high De , as seen in Figs. 4(c, d). The presence of a thin stress boundary layer on the surface of the cylinder and elongation in the region of stagnation points causes a significant pressure difference around it, as reported in the literature [39]. The

fluid behaviour closely approaches that of a Newtonian fluid at lower values of De , and thus the pressure contours show similarity with those seen in Newtonian fluid flow. At low Deborah numbers, the pressure exhibits nearly symmetrical contours. However, as the Deborah number increases, the pressure contours undergo distortion in the vicinity of the cylinder. At high De (Fig. 4(c, d)), a protrusion arises at the rear side of the cylinder. As β decreases from 0.9 to 0.1, a protrusion that was initially flatter becomes more pointed and enlarges.

Subsequently, Fig. 5 illustrates the scaled first normal stress difference ($N_1 = \tau_{xx} - \tau_{yy}$) contours around the cylinder for the extreme values of the Deborah number (De) and the solvent viscosity ratio (β). Uniformly distributed ($\delta N_1 = 5$) contour lines ranging from $N_{1,\min} = -550$ to $N_{1,\max} =$

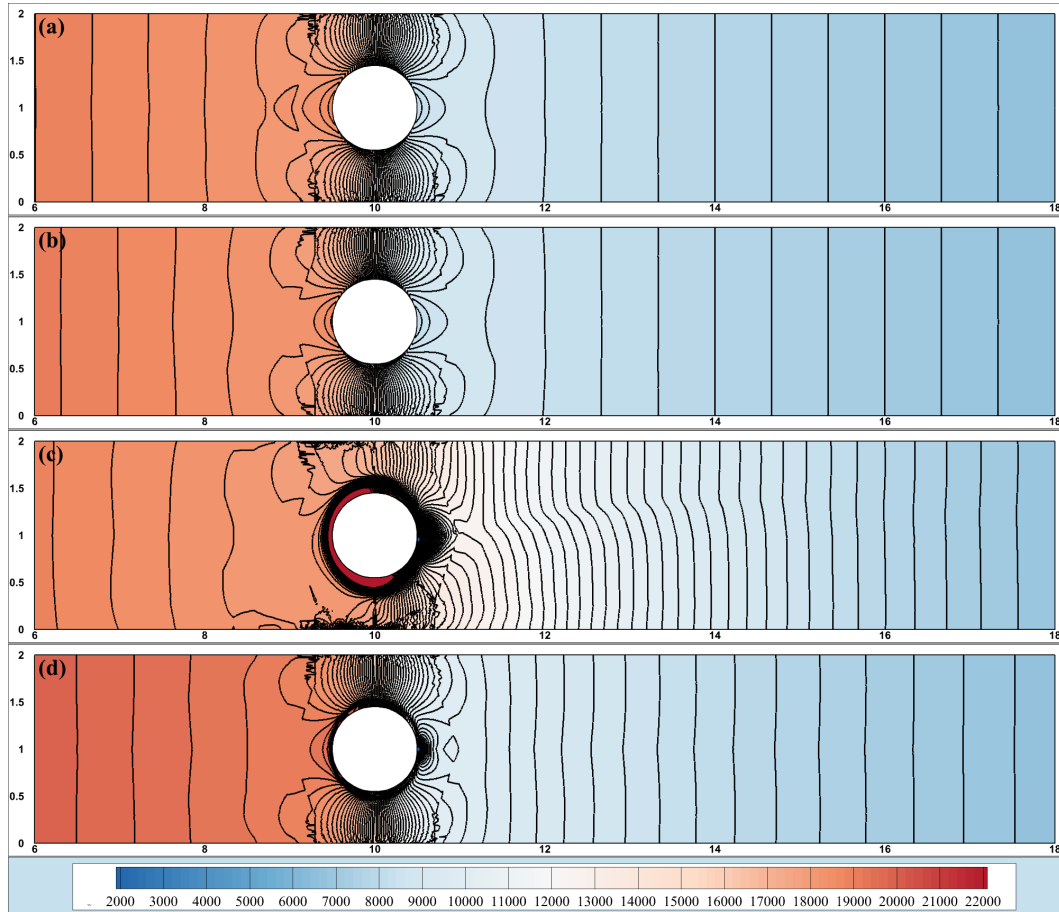


Figure 4: Pressure (p) contours around the cylinder for (a) $De = 0.025$, $\beta = 0.1$ (b) $De = 0.025$, $\beta = 0.9$ (c) $De = 1.5$, $\beta = 0.1$ (d) $De = 1.5$, $\beta = 0.9$

50 are drawn in Fig 5. The profiles display a complex dependence of the stress on the dimensional parameters (De , β). For instance, in Fig. 5(a), where De is low, and β is high, there is no induced polymeric effect, and the flow is very similar to that of Newtonian fluid. The stress (N_1) contours are only concentrated at the surface of the cylinder. With increasing β , at fixed De , the polymeric effect tends to induce, and the effects get carried away from the surface of the cylinder to the surrounding regions, as seen in Fig. 5(b). Further, with an increase in De , refer Fig. 5(c,d), the stress wake enlarges and spans almost the whole length of the channel, and a thin stress boundary layer forms on the surface of a cylinder. These observations agree with the results reported [39].

5.4. Coefficient of pressure

Fig. 6 depicts the pressure coefficient (C_p , defined in Eq. 17) profiles on the surface ($0^\circ \leq \theta \leq 360^\circ$) of the cylinder for the considered ranges of β and De . Here, $\theta = 180^\circ$ indicates the front stagnation point (FSP), and $\theta = 0^\circ$ (or 360°) represents the rear stagnation point (RSP) on the

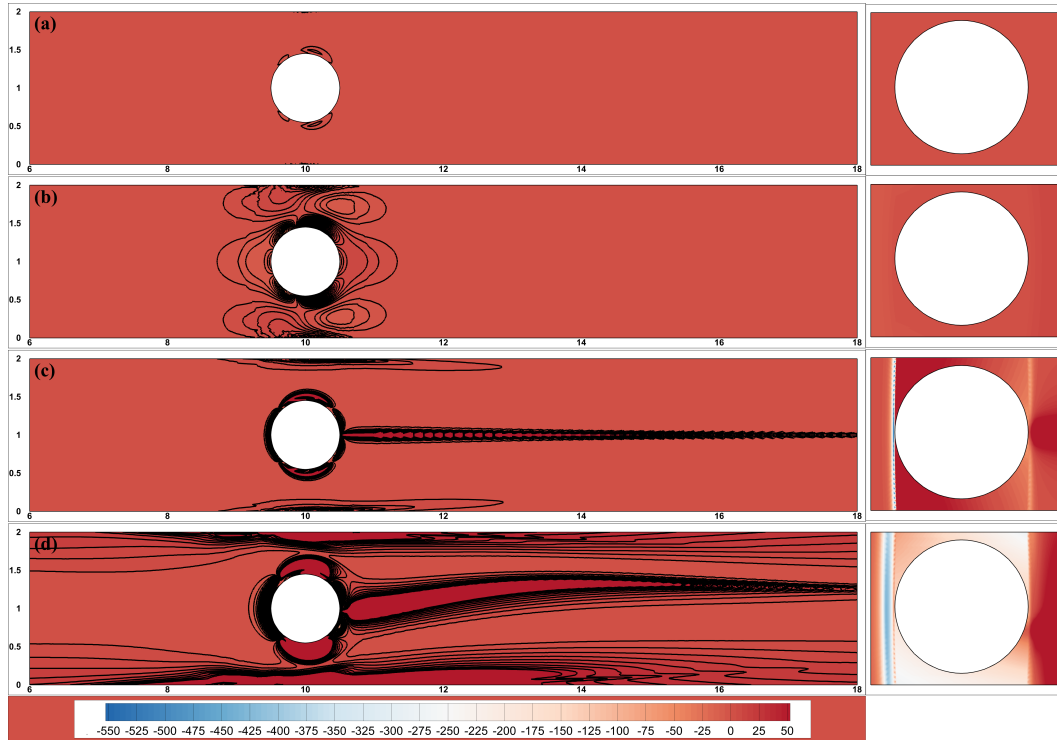


Figure 5: First normal stress difference ($N_1 = \tau_{xx} - \tau_{yy}$) contours around the cylinder for (a) $De = 0.025$, $\beta = 0.9$ (b) $De = 0.025$, $\beta = 0.1$ (c) $De = 1.5$, $\beta = 0.9$ (d) $De = 1.5$, $\beta = 0.1$

surface of the cylinder. The C_p profiles are qualitatively consistent, at the lower values of De and β , with the literature [25, 63] on Newtonian and non-Newtonian power-law fluid flowing across a cylinder. Broadly, C_p profiles are symmetric in the upper and lower half of the cylinder, as expected, due to the creeping nature of the flow. For the fixed values of β and De , C_p increases from the minimum value at RSP ($\theta = 0^\circ$) until it reaches its peak at the FSP ($\theta = 180^\circ$) of the cylinder, and, after that, it starts decreasing until RSP ($\theta = 360^\circ$). For lower values of De and β , C_p decreases in the frontal side of the cylinder, and subsequently, the curve flattens in the rear side of the cylinder as the polymeric effects tend to dominate, and the boundary layer thickness may increase. A thicker boundary layer leads to a slower velocity near the surface of the cylinder. This deceleration of the flow near the frontal side of the cylinder decreases in

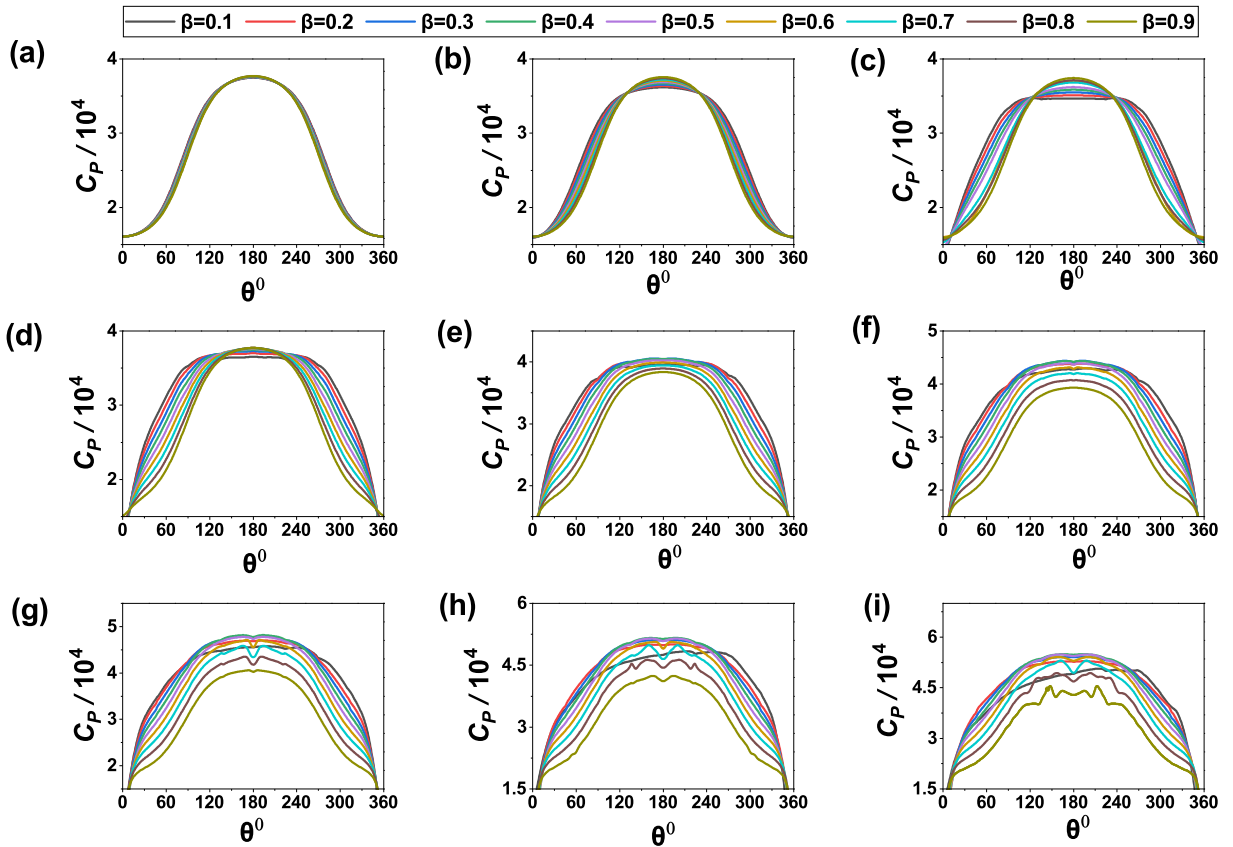


Figure 6: Variation of C_p over the surface ($0^\circ \leq \theta \leq 360^\circ$) of the cylinder for $0.1 \leq \beta \leq 0.9$ at (a) $De = 0.025$ (b) $De = 0.1$ (c) $De = 0.3$ (d) $De = 0.5$ (e) $De = 0.7$ (f) $De = 0.9$ (g) $De = 1.1$ (h) $De = 1.3$ (i) $De = 1.5$.

that region. Due to the above-specified reason, crossing over in C_p profiles is seen in Fig. 6(a-d). However, at higher values of De , the viscoelastic effects tend to dominate, which affects the symmetry of the C_p profiles, especially for the higher values of β due to the additional polymeric effects. Furthermore, it is clearly illustrated in Fig. 7 that the influence of β is comparatively less pronounced at lower De but has significant effect at higher De .

Subsequently, Fig. 7 illustrates C_p profile over a vertical line A (x_c, y) that passes through the center of the cylinder (refer Fig. 1). The discontinuity shown on the x -axis of Fig. 7 denotes the region ($0.5 \leq y \leq 1.5$) overlapped with the cylinder. The profiles clearly show that the value of C_p increases from the channel wall ($y = 0$ or H) up to the surface ($y = 0.5$ and 1.5) of the

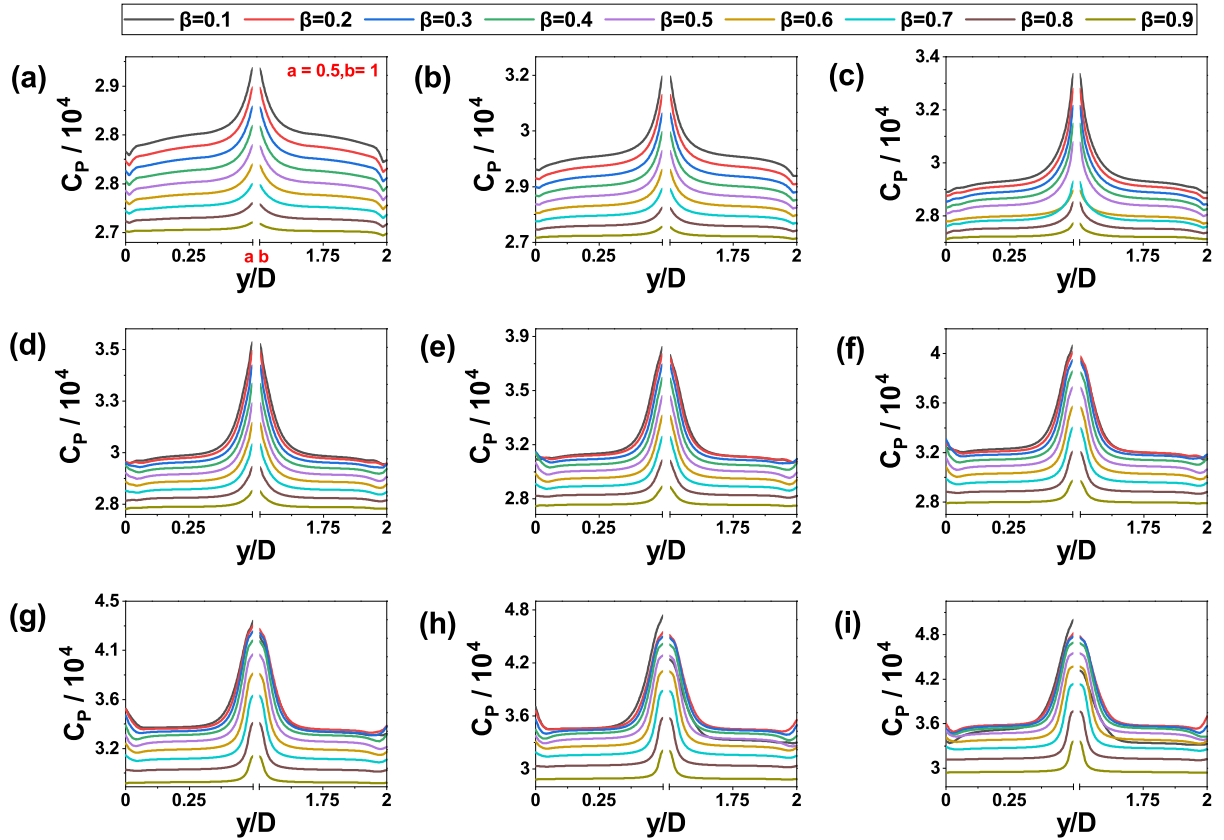


Figure 7: Variation of C_p along line A (x_c, y), (refer Fig. 1) for different β at (a) $De = 0.025$ (b) $De = 0.1$ (c) $De = 0.3$ (d) $De = 0.5$ (e) $De = 0.7$ (f) $De = 0.9$ (g) $De = 1.1$ (h) $De = 1.3$ (i) $De = 1.5$.

cylinder. Furthermore, C_p values decrease with increasing β for a given Deborah number (De). Interestingly, C_p assumes greater values for lower β at a lower Deborah number ($De \leq 0.7$).

5.5. Wall shear stress (WSS)

Fig. 8 displays the variation of magnitude of the wall shear stress (WSS, $|\tau_w/\tau_0|$) over the surface ($0^\circ \leq \theta \leq 360^\circ$) of the cylinder over the ranges of considered conditions (β , De). At both RSP ($\theta = 0^\circ$) and FSP ($\theta = 0^\circ$ and 360°), the magnitude of WSS becomes zero (i.e., $|\tau_w/\tau_0| = 0$) due to velocity gradient being zero as the kinetic energy completely converts to the potential energy without any loss of energy at the stagnation point. In general, WSS displays a symmetric nature in the upper ($0^\circ \leq \theta \leq 180^\circ$) and lower ($180^\circ \leq \theta \leq 360^\circ$) half of the cylinder. At low

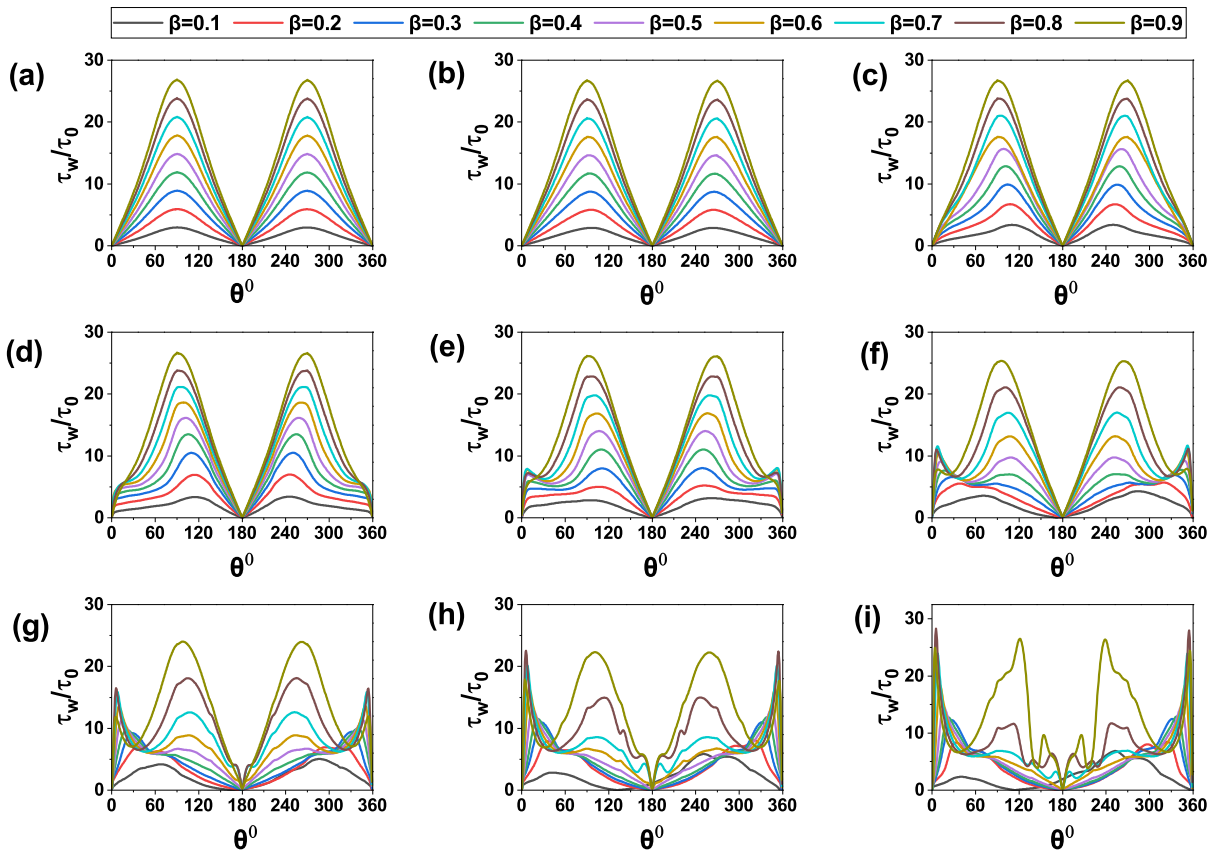


Figure 8: Variation of WSS ($|\tau_w/\tau_0|$) over the surface of the cylinder for different β at (a) $De = 0.025$ (b) $De = 0.1$ (c) $De = 0.3$ (d) $De = 0.5$ (e) $De = 0.7$ (f) $De = 0.9$ (g) $De = 1.1$ (h) $De = 1.3$ (i) $De = 1.5$.

$De \leq 0.1$, in the upper half ($0^\circ \leq \theta \leq 180^\circ$), WSS increases upward from RSP to top ($\theta = 90^\circ$), subsequently decreasing up to the FSP; the vice versa is seen in the lower half ($360^\circ \geq \theta \geq 180^\circ$) of the cylinder, as seen in Fig. 8(a, b). WSS has shown the highest and equal magnitude at the top ($\theta = 90^\circ$) and bottom ($\theta = 270^\circ$) of the cylinder, as the velocity gradient gets maximized at these locations due to their close proximity to the channel wall. With increasing De , while the symmetry in the profiles remains, the peak of the curves shifts towards FSP, Fig. 8(c, d), and additional minor peaks appear near RSP with decreasing β , Fig. 8(e, g). The high polymeric effect (i.e., lower β) attributes in the flattening of WSS profiles for smaller β values at high (De). There is a sudden spike in the value of WSS at the frontal side of the cylinder at higher De and lower β , as indicated in Fig. 8(e - i). At higher De and lower values of β , Fig. 8(g - i), the profiles are no more symmetrical, and the value of WSS is higher on the bottom than at the top of the cylinder. One of the potential causes of the phenomena mentioned above could be the start of the wake development at the top side of the cylinder, which may have decreased the WSS there.

5.6. Normal Stress

Fig. 9 shows the variation of the normal component of stress (τ_{xx}/τ_0) over the surface ($0^\circ \leq \theta \leq 360^\circ$) the cylinder. The normal stress has shown significant dependence on the governing parameters (De, β), as compared with WSS (Fig. 8). The profiles have shown two peaks, each at the top and bottom sides of the cylinder, due to the thinning of the boundary layer. The maximum value of τ_{xx} increases with De as the viscoelastic effect tends to dominate, and there is an increase in the relaxation time. At a particular De , τ_{xx} increases with a decrease in β as the polymeric effects dominate; it increases the induced stress. As expected, τ_{xx} is zero at FSP and RSP. It can be seen in Fig. 9(a), τ_{xx} value deviates from zero and becomes negative on the upper and lower sides of the front portion of the cylinder at lower De . However, at higher De , τ_{xx} values are higher on the lower side of the cylinder than the upper side, especially for lower β .

Furthermore, the existing literature [64] suggests that the contribution of the flow-dependent

normal stress is much higher than the contribution of the flow-dependent shear stress. Fig. 10 describes the variation of normal stress difference (N_1/τ_0) over the cylinder surface. A comparison of Figs. 8 and 9 clearly state that the normal stress (τ_{xx}) is much more dominated as compared to WSS (τ_w). As the De increases, a dip in the profiles at RSP ($\theta = 0^\circ$) clearly indicates the dominance of τ_{yy} at that location. Also, at higher De , there is a flat profile with lower values of normal stress difference for lower β , which indicates that τ_{xx} and τ_{yy} components of stress are balanced at FSP. But at lower β , as the polymeric effect tends to dominate, there is great dominance of τ_{xx} component of stress.

Further, Fig. 11 depicts the variation of the first normal stress difference (N_1/τ_0) over the line A

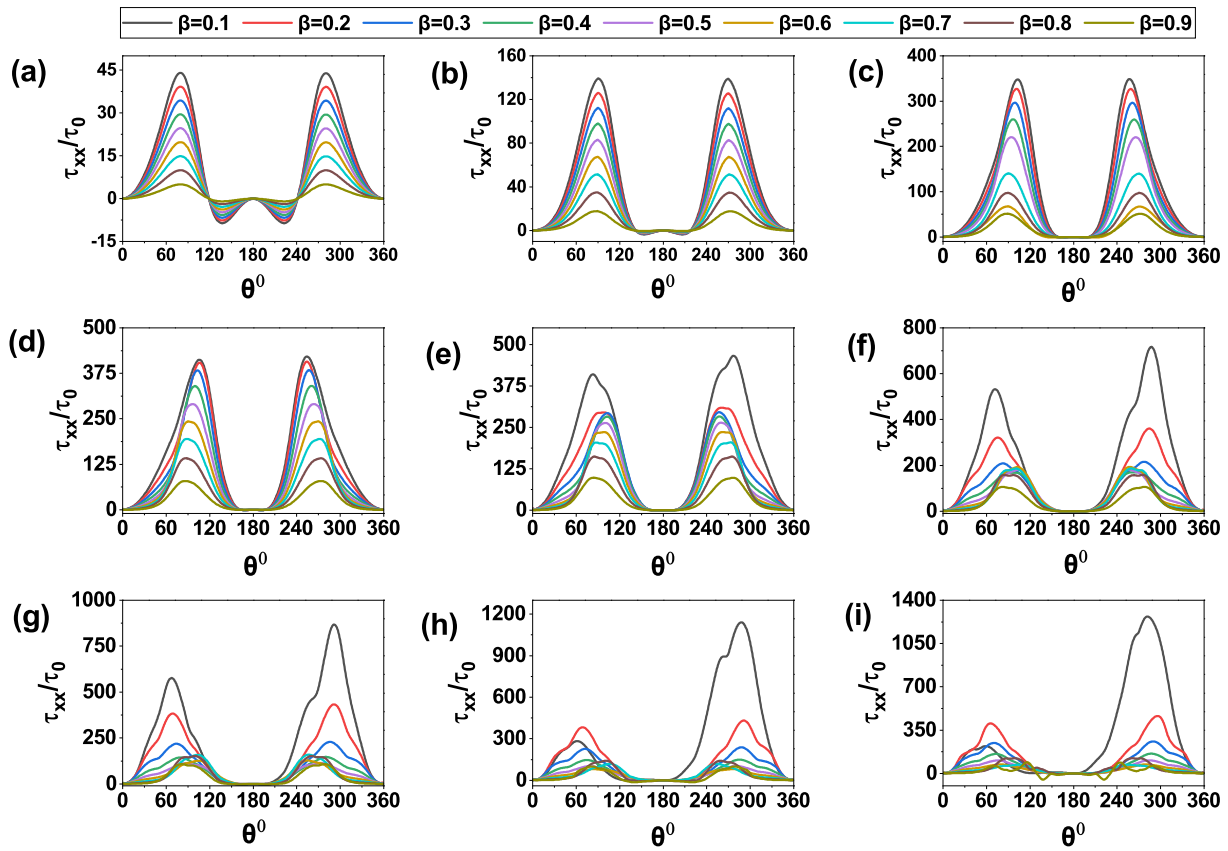


Figure 9: Variation of normal component of stress (τ_{xx}/τ_0) over the surface ($0^\circ \leq \theta \leq 360^\circ$) of the cylinder for different β at (a) $De = 0.025$ (b) $De = 0.1$ (c) $De = 0.3$ (d) $De = 0.5$ (e) $De = 0.7$ (f) $De = 0.9$ (g) $De = 1.1$ (h) $De = 1.3$ (i) $De = 1.5$.

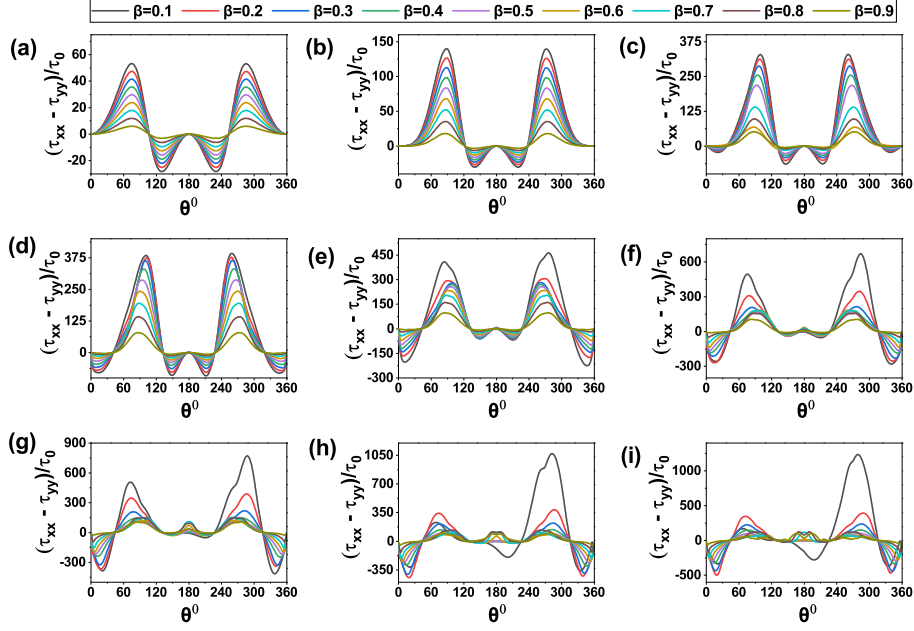


Figure 10: Variation of first normal stress difference (N_1/τ_0) over the surface ($0^\circ \leq \theta \leq 360^\circ$) of the cylinder for different β at (a) $De = 0.025$ (b) $De = 0.1$ (c) $De = 0.3$ (d) $De = 0.5$ (e) $De = 0.7$ (f) $De = 0.9$ (g) $De = 1.1$ (h) $De = 1.3$ (i) $De = 1.5$.

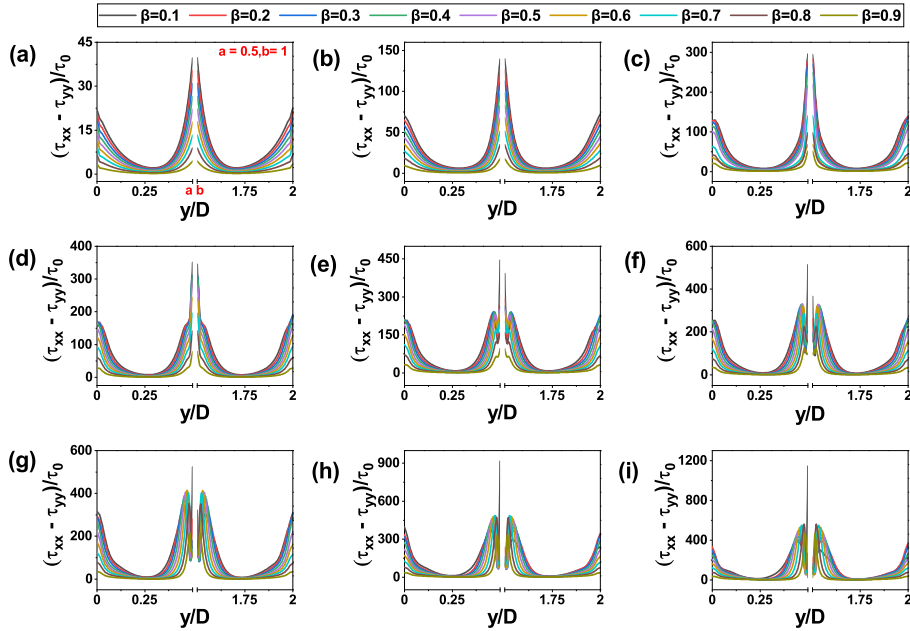


Figure 11: Variation of normal stress difference (N_1/τ_0) along line A (x_c, y), (refer Fig. 1) for different β at (a) $De = 0.025$ (b) $De = 0.1$ (c) $De = 0.3$ (d) $De = 0.5$ (e) $De = 0.7$ (f) $De = 0.9$ (g) $De = 1.1$ (h) $De = 1.3$ (i) $De = 1.5$.

(refer Fig. 1) for the considered ranges of conditions (β , De). As expected, N_1 values are larger near the channel wall and adjacent to the cylinder surface on both the upper and lower sides of the cylinder, and the values reduce between the gap, due to the solid and stationary walls. The larger values are obtained adjacent to the cylinder surface at lower values of β and De ; however, increasing De shows complex trends consistent with the above-discussed findings.

5.7. Velocity

Subsequently, Fig. 12 depicts the variation of the x -component of the velocity (u_x/U_{avg}) over the line A (refer Fig. 1) for the considered ranges of conditions (β , De). As both channel wall and cylinder are no-slip and impermeable, the velocity appears zero ($u_x = 0$) at these locations in

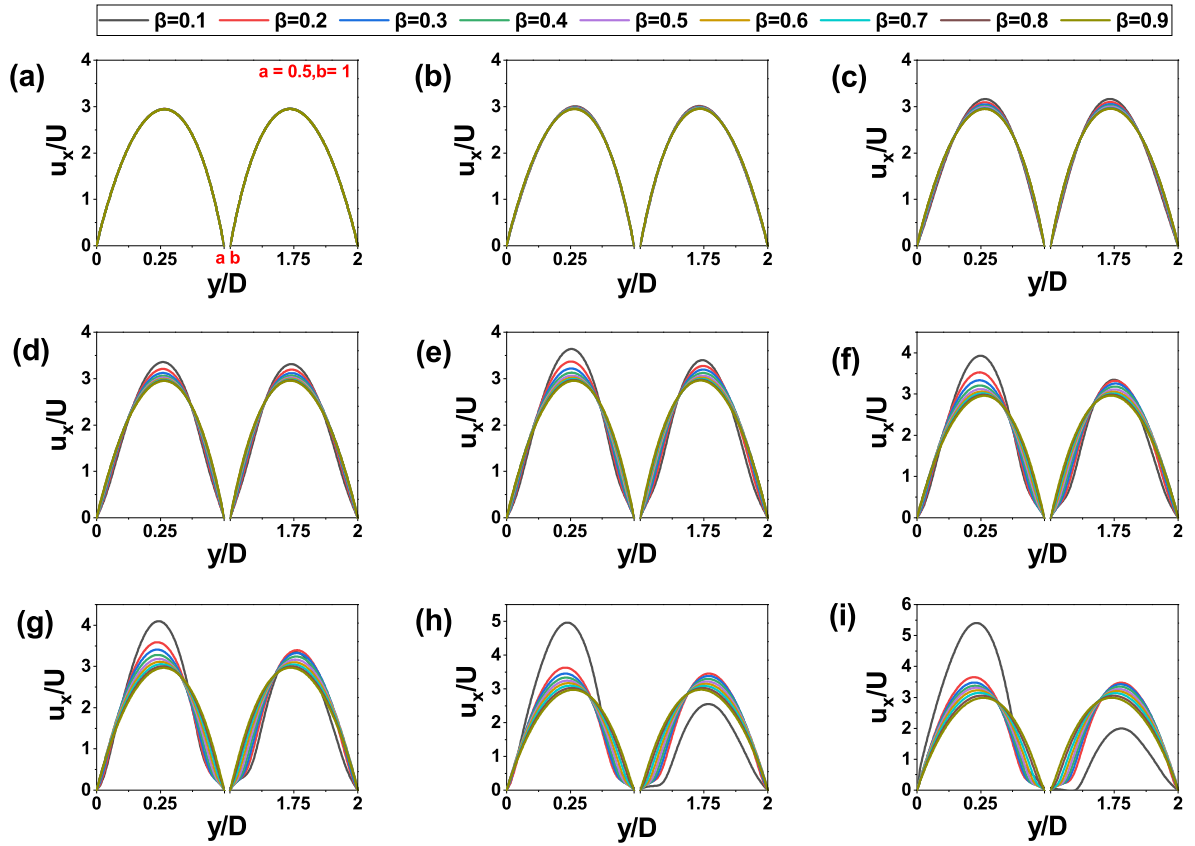


Figure 12: Velocity profile along line A (x_c, y), (refer Fig. 1) for different β at (a) $De = 0.025$ (b) $De = 0.1$ (c) $De = 0.3$ (d) $De = 0.5$ (e) $De = 0.7$ (f) $De = 0.9$ (g) $De = 1.1$ (h) $De = 1.3$ (i) $De = 1.5$.

Fig. 12. Further, the similar profiles for lower $De \leq 0.9$ in the upper and lower sides of the cylinder, refer Fig. 12, deviate with increasing De . The velocity increases between the gap, in both upper and lower sides of the cylinder, due to decreasing flow area for fixed volumetric flow. The velocity profiles, therefore, appear parabolic, especially for lower De , with minor deviations at higher De . It is noteworthy evident through two peaks in each profile. The velocity remains unaffected by β for low $De \leq 0.3$. Nevertheless, at progressively higher Deborah numbers (De), lower β values negatively affect become on the lower region of the cylinder compared to the upper region. Furthermore, the velocity in the lower gap is significantly reduced compared to the same in the upper gap. Also, the velocity gradient at the surface of the cylinder decreases for low β values at higher De .

5.8. Drag Characteristics

The above sections have depicted the stronger role of flow governing parameters (De, β) of the local flow behavior, such as streamline and stress contour profiles, line profiles for the wall shear stress, pressure coefficient, normal stress, first normal stress difference, and velocity. Subsequently, the global engineering parameters, such as the drag coefficient, are analyzed in this section to understand the influence of these complex local flow characteristics manipulated by the governing parameters (β, De). In general, the total drag coefficient (C_D) is a contribution of the pressure drag coefficient (C_{DP}), and the viscous drag coefficient (C_{DF}), as defined in Eq. (15). Figure 13 illustrates the dependence of the drag coefficient and its component ($C_D, C_{DP}, C_{DF}, C_{DP}/C_{DF}$) on the Deborah number (De) and solvent viscosity ratio (β).

Fig. 13(a) shows the dependence of pressure drag coefficient (C_{DP}) on the governing parameters (De, β). For a fixed value of β , as the Deborah number increases gradually, initially, C_{DP} decreases up to $De = 0.3$, after that, it increases, and the increase is much more significant at higher β . For lower values of $De (\leq 0.7)$, the pressure drag coefficient (C_{DP}) decreases as β decreases. However, at higher values of De , the dependence of C_{DP} on β becomes rather complex; this may be attributed to as the relaxation time (λ) increases, viscoelastic effects

enhance, and thus the polymeric nature complexly influence C_{DP} . Furthermore, at the higher value of Deborah number (De), there is a strong dependence of C_{DP} on the solvent viscosity ratio (β).

Fig. 13(b) shows the dependence of friction drag coefficient (C_{DF}) on the governing parameters (De , β). For a fixed value of Deborah number (De), the viscous drag coefficient (C_{DF}) decreases with a decrease in β . For a fixed β , C_{DF} decreases with an increase in De , as the relaxation time and polymeric effect increase, the fluid remains attached to the cylinder for a more extended period, thus lowering the C_{DF} . Further, at higher De , C_{DF} values are almost equal for lower values of $\beta \leq 0.7$. This phenomenon may be attributed to the increased polymeric effects with

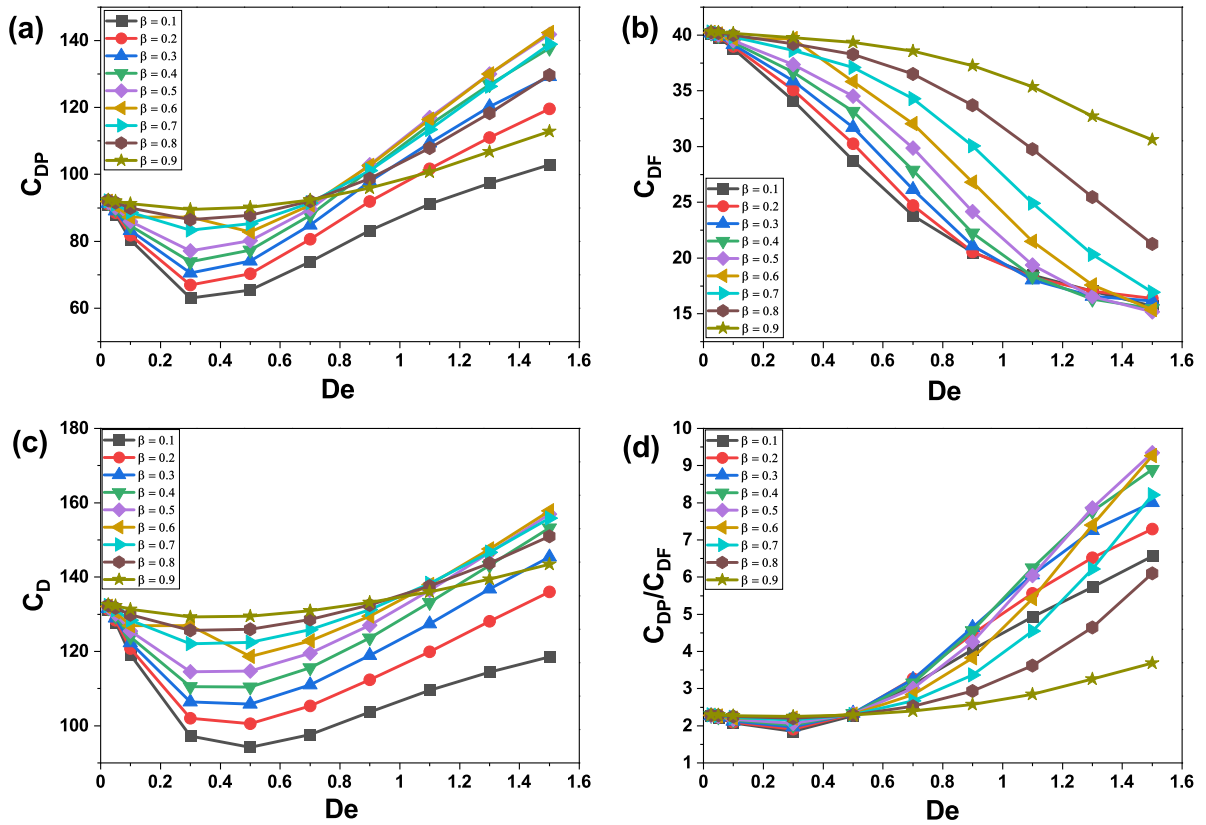


Figure 13: Dependence of the (a) pressure drag coefficient C_{DP} (b) friction drag coefficient C_{DF} (c) total drag coefficient C_D (d) the drag ratio $C_{DR} = C_{DP}/C_{DF}$ on the Deborah number (De) and solvent viscosity ratio (β).

decreasing β . As discussed with C_{DP} , the fluid remains attached to the cylinder for an extended time. Hence, there is no significant change in C_{DF} value.

Subsequently, Fig. 13(c) shows the dependence of total drag coefficient (C_D) on the governing parameters (De, β). Qualitatively, the total drag coefficient (C_D) trends are similar to that of the pressure drag coefficient (C_{DP}). With increasing De , initially, there is a decrease in the value of C_D upto $De = 0.5$ for $De \leq 0.5$, and then it starts to increase. For lower values of $De \leq 0.9$, as the value of β increases, there is an increase in C_D due to dominating C_{DP} . For higher values of De , the dependence of C_D upon β is complex, but it still follows the trend at lower β . At lower De , the value of C_D is almost same, but for the moderate De (say 0.7), there is a 34.04% increase in C_D as the β is increased from 0.1 to 0.9. However, at $De = 1.5$, there is a 20.99% increase in C_D as β is varied from 0.1 to 0.9.

Furthermore, to analyze the relative importance of the individual drag components, Fig. 13(d) shows the dependence of drag ratio ($C_{DR} = C_{DP}/C_{DF}$) on the governing parameters (De, β). As indicated from C_{DP} and C_{DF} , the drag ratio appears to be greater than 1 (i.e., $C_{DR} > 1$) for the ranges of De and β suggesting the dominance of pressure forces in this flow. Further, the dominance of pressure drag is more pronounced at the higher Deborah number (De). Overall, the drag characteristics are complexly influenced by the flow governing parameters (De, β).

6. Conclusions

In this study, the hydrodynamics of Oldroyd-B fluid flowing around a channel confined circular cylinder is investigated numerically. The numerical modeling and simulations are performed using the finite volume method open-source CFD solver, rheoTool based on OpenFOAM, for the following ranges of conditions: Deborah number ($0.025 \leq De \leq 1.5$), solvent viscosity ratio ($0.1 \leq \beta \leq 0.9$), blockage ratio ($B = 0.5$) under the creeping flow (Reynolds number, $Re = 0.01$) regime. The detailed kinematics in terms of the streamline, pressure and stress contour profiles, and engineering parameters as drag coefficient have been presented and discussed. Further detailed kinematics understandings are gained by analyzing the line plots for

pressure coefficients, wall shear stress, normal stress, and normal stress difference over the surface of the cylinder and on the vertical line in the gap between the cylinder and the channel wall. For lower De , we can see that the contours of the flow field contour profiles are perfectly symmetric for all values of β . However, at higher values of De , the flow contours show asymmetric behavior at lower β where the polymeric effects are significant, indicating a difference in flow pattern at the top and bottom side of the cylinder. The line plots in between the gap have shown the symmetric flow in both the top and bottom sides of the cylinder at lower De ; the symmetry is lost with increasing De , particularly at lower β . Further, both De and β have a significant influence on the drag coefficient and its components (C_{DP}, C_{DF}, C_D). At lower De , C_D value is almost same irrespective of β but as we move to higher De ($=1.5$) there is a 20.99 % increment in C_D value as β is increased from 0.1 to 0.9 at higher De ($=1.5$). With an increase in β at high De , the fluid transitions from elastic to viscous nature, leading to a subsequent rise in the drag coefficient. Over the range of parameters, the pressure drag force dominates over the frictional drag force in the flow. Overall, at lower De , the influence of β is less prominent but at higher value of De , the influence of β is significant.

CRedit Authors Contributions Statement

In this work, the authors contributed as follows.

Author No.	Author Name	Contribution
1	Pratyush Kumar Mohanty	Open-source Software, Investigation, Data Curation, Validation, Visualization, Formal analysis, Writing - Original Draft
2	Akhilesh Kumar Sahu	Supervision, Conceptualization, Methodology, Resources, Formal analysis, Writing - Review & Editing
3	Ram Prakash Bharti	Supervision, Conceptualization, Methodology, Resources, Open-source Software, Formal analysis, Writing - Review & Editing

Declaration of Competing Interest

The authors declare that they have no known competing financial interests or personal relationships that could have appeared to influence the work reported in this paper.

Acknowledgements

P.K. Mohanty would like to acknowledge the internship opportunity at the Complex Fluid Dynamics and Microfluidics (CFDM) Lab, Department of Chemical Engineering, Indian Institute of Technology Roorkee, India.

Nomenclature

B	Blockage ratio, dimensionless
C_p	Coefficient of pressure, dimensionless
C_{DF}	Viscous component of drag coefficient, dimensionless
C_{DP}	Pressure component of drag coefficient, dimensionless
C_D	Total drag coefficient, dimensionless
D	Diameter of the cylinder (m)
De	Deborah number, dimensionless
F_D	Drag force per unit length of the cylinder (N/m)
H	Height of the computational domain, dimensionless
I	Identity tensor, dimensionless
L	Length of the computational domain, dimensionless
L_d	Downstream length of the computational domain, dimensionless
L_u	Upstream length of the computational domain, dimensionless
p	Pressure (Pa)

Re	Reynolds number, dimensionless
u_x	Velocity in x-direction (m/s)
u_y	Velocity in y-direction (m/s)
U_{avg}	Average inlet velocity (m/s)
x	Stream-wise coordinate (m)
y	Transverse coordinate (m)

Greek Symbols

β	Solvent viscosity ratio, dimensionless
η_0	Total viscosity (Pa.s)
η_p	Polymeric viscosity (Pa.s)
η_s	Solvent viscosity (Pa.s)
λ	Relaxation time (s)
ρ	Density of the fluid (Kg/m^3)
τ	Total extra-stress tensor (Pa)
τ_p	Polymeric contribution in the extra-stress tensor (Pa)
τ_s	Solvent contribution in the extra-stress tensor (Pa)

Abbreviations

CFD	Computational Fluid Dynamics
CUBISTA	Convergent and Universally Bounded Interpolation Scheme for Treatment of Advection
DAVSS	Discrete Adaptive Elastic Viscous Split Stress
DILU	Diagonal based Incomplete LU
PBiCG	Preconditioned Biconjugate Gradient
SIMPLE	Semi Implicit Pressure Linked Equation

References

- [1] V. L. Streeter, **Handbook of Fluid Dynamics**, McGraw-Hill, New York, 1961.
- [2] R. W. Johnson (Ed.), **Handbook of Fluid Dynamics**, CRC Press, 2nd edn., 2016.
- [3] U. Ghosh, S. Upadhyay, R. Chhabra, Heat and Mass Transfer from Immersed Bodies to Non-Newtonian Fluids, in: J. P. Hartnett, T. F. Irvine, Y. I. Cho, G. A. Greene (Eds.), **Advances in Heat Transfer**, vol. 25 of *Advances in Heat Transfer*, Elsevier, 251–319, 1994.
- [4] Z. Zapryanov, S. Tabakova, **Dynamics of Bubbles, Drops and Rigid Particles**, Springer Netherlands, 1999.
- [5] M. M. Zdravkovich, **Flow Around Circular Cylinders. Volume 1: Fundamentals**, Oxford university press, 1997.
- [6] M. M. Zdravkovich, **Flow Around Circular Cylinder. Volume 2: Applications**, Oxford university press, 2003.
- [7] R. Clift, J. R. Grace, M. E. Weber, **Bubbles, Drops, and Particles**, Dover Publications, New York, 2005.
- [8] E. E. Michaelides, **Particles, Bubbles and Drops: Their Motion, Heat and Mass Transfer**, World Scientific, 2006.
- [9] R. Chhabra, Fluid Flow and Heat Transfer from Circular and Noncircular Cylinders Submerged in Non-Newtonian Liquids, in: Y. I. Cho, G. A. Greene (Eds.), **Advances in Heat Transfer**, vol. 43 of *Advances in Heat Transfer*, Elsevier, 289–417, 2011.
- [10] R. P. Chhabra, S. A. Patel, **Bubbles, Drops, and Particles in Non-Newtonian Fluids**, CRC Press, 2023.
- [11] E. Loth, **Fluid Dynamics of Particles, Drops, and Bubbles**, Cambridge University Press, 2023.
- [12] R. B. Bird, R. C. Armstrong, O. Hassager, **Dynamics of Polymeric Liquids. Vol. 1: Fluid mechanics**, John Wiley and Sons Inc., New York, 1987.
- [13] R. P. Chhabra, J. F. Richardson, **Non-Newtonian Flow and Applied Rheology: Engineering Applications**, Butterworth-Heinemann, 2011.
- [14] A. W. Liu, D. E. Bornside, R. C. Armstrong, R. A. Brown, Viscoelastic flow of polymer solutions around a periodic, linear array of cylinders: comparisons of predictions for microstructure and flow fields, **Journal of Non-Newtonian Fluid Mechanics** 77 (3) (1998) 153–190.
- [15] G. H. McKinley, R. C. Armstrong, R. Brown, The wake instability in viscoelastic flow past confined circular cylinders, **Philosophical Transactions of the Royal Society of London. Series A: Physical and Engineering Sciences** 344 (1671) (1993) 265–304.
- [16] F. Hamid, C. Sasmal, Significant influence of fluid viscoelasticity on flow dynamics past an oscillating cylinder, **Journal of Fluid Mechanics** 975 (2023) A26.
- [17] C. H. K. Williamson, Vortex dynamics in the cylinder wake, **Annual Review of Fluid Mechanics** 28 (1) (1996) 477–539, ISSN 1545-4479.
- [18] H. Choi, W.-P. Jeon, J. Kim, Control of flow over a bluff body, **Annual Review of Fluid Mechanics** 40 (1) (2008) 113–139, ISSN 1545-4479.

- [19] L. Zovatto, G. Pedrizzetti, Flow about a circular cylinder between parallel walls, *Journal of Fluid Mechanics* 440 (2001) 1–25.
- [20] J. Chakraborty, N. Verma, R. Chhabra, Wall effects in flow past a circular cylinder in a plane channel: a numerical study, *Chemical Engineering and Processing: Process Intensification* 43 (12) (2004) 1529–1537.
- [21] S. Mettu, N. Verma, R. Chhabra, Momentum and heat transfer from an asymmetrically confined circular cylinder in a plane channel, *Heat and Mass Transfer* 42 (11) (2006) 1037–1048.
- [22] S. Singha, K. Sinhamahapatra, Flow past a circular cylinder between parallel walls at low Reynolds numbers, *Ocean Engineering* 37 (8-9) (2010) 757–769.
- [23] M. Sahin, R. G. Owens, A numerical investigation of wall effects up to high blockage ratios on two-dimensional flow past a confined circular cylinder, *Physics of Fluids* 16 (5) (2004) 1305–1320.
- [24] S. K. Mishra, S. Sen, A. Verma, Steady flow past a circular cylinder under large blockage, *European Journal of Mechanics-B/Fluids* 87 (2021) 135–150.
- [25] R. P. Bharti, R. P. Chhabra, V. Eswaran, Two-dimensional steady Poiseuille flow of power-law fluids across a circular cylinder in a plane confined channel: wall effects and drag coefficients, *Industrial & Engineering Chemistry Research* 46 (11) (2007) 3820–3840.
- [26] R. P. Bharti, R. Chhabra, V. Eswaran, Effect of blockage on heat transfer from a cylinder to power law liquids, *Chemical Engineering Science* 62 (17) (2007) 4729 – 4741.
- [27] M. Rao, A. K. Sahu, R. Chhabra, Effect of confinement on power-law fluid flow past a circular cylinder, *Polymer Engineering & Science* 51 (10) (2011) 2044–2065.
- [28] S. Bijjam, A. K. Dhiman, CFD analysis of two-dimensional non-Newtonian power-law flow across a circular cylinder confined in a channel, *Chemical Engineering Communications* 199 (6) (2012) 767–785.
- [29] S. Bijjam, A. Dhiman, V. Gautam, Laminar momentum and heat transfer phenomena of power-law dilatant fluids around an asymmetrically confined cylinder, *International Journal of Thermal Sciences* 88 (2015) 110–127.
- [30] G. Vishal, J. Tomar, R. P. Bharti, Critical parameters for non-Newtonian shear-thickening power-law fluids flow across a channel confined circular cylinder, *Journal of the Taiwan Institute of Chemical Engineers* 123 (2021) 34–46.
- [31] P. Sivakumar, R. P. Bharti, R. P. Chhabra, Effect of power-law index on critical parameters for power-law flow across an unconfined circular cylinder, *Chemical Engineering Science* 61 (18) (2006) 6035 – 6046.
- [32] A. E. Caola, Y. Joo, R. Armstrong, R. Brown, Highly parallel time integration of viscoelastic flows, *Journal of Non-Newtonian Fluid Mechanics* 100 (1-3) (2001) 191–216.
- [33] R. G. Owens, C. Chauvière, T. N. Philips, A locally-upwinded spectral technique (LUST) for viscoelastic flows,

- Journal of Non-Newtonian Fluid Mechanics* 108 (1-3) (2002) 49–71.
- [34] J. M. Kim, C. Kim, K. H. Ahn, S. J. Lee, An efficient iterative solver and high-resolution computations of the Oldroyd-B fluid flow past a confined cylinder, *Journal of Non-Newtonian Fluid Mechanics* 123 (2-3) (2004) 161–173.
- [35] M. A. Hulsen, R. Fattal, R. Kupferman, Flow of viscoelastic fluids past a cylinder at high Weissenberg number: stabilized simulations using matrix logarithms, *Journal of Non-Newtonian Fluid Mechanics* 127 (1) (2005) 27–39.
- [36] M. A. Carrozza, M. A. Hulsen, M. Hütter, P. D. Anderson, Viscoelastic fluid flow simulation using the contravariant deformation formulation, *Journal of Non-Newtonian Fluid Mechanics* 270 (2019) 23–35.
- [37] P. J. Oliveira, F. d. Pinho, G. Pinto, Numerical simulation of non-linear elastic flows with a general collocated finite-volume method, *Journal of Non-Newtonian Fluid Mechanics* 79 (1) (1998) 1–43.
- [38] M. A. Alves, F. T. Pinho, P. J. Oliveira, The flow of viscoelastic fluids past a cylinder: finite-volume high-resolution methods, *Journal of Non-Newtonian Fluid Mechanics* 97 (2-3) (2001) 207–232.
- [39] H.-S. Dou, N. Phan-Thien, Viscoelastic flow past a confined cylinder: Instability and velocity inflection, *Chemical Engineering Science* 62 (15) (2007) 3909–3929.
- [40] D. Richter, G. Iaccarino, E. S. G. Shaqfeh, Simulations of three-dimensional viscoelastic flows past a circular cylinder at moderate Reynolds numbers, *Journal of Fluid Mechanics* 651 (2010) 415–442, ISSN 1469-7645.
- [41] A. Minaeian, M. Nili-Ahmadabadi, M. Norouzi, Numerical study of Phan-Thien-Tanner viscoelastic fluid flow around a two-dimensional circular cylinder at a low Reynolds number: a new classification for drag variations regimes, *Meccanica* 54 (11–12) (2019) 1717–1745, ISSN 1572-9648.
- [42] A. Minaeian, M. Nili-AhmadAbadi, M. Norouzi, K. C. Kim, Effects of viscoelasticity on the onset of vortex shedding and forces applied on a cylinder in unsteady flow regime, *Physics of Fluids* 34 (2022) 013106.
- [43] C. C. Hopkins, S. J. Haward, A. Q. Shen, Upstream wall vortices in viscoelastic flow past a cylinder, *Soft Matter* 18 (2022) 4868–4880.
- [44] M. Kumar, A. M. Ardekani, Hysteresis in viscoelastic flow instability of confined cylinders, *Phys. Rev. Fluids* 7 (2022) 093302.
- [45] J. G. Oldroyd, On the formulation of rheological equations of state, *Proceedings of the Royal Society of London. Series A. Mathematical and Physical Sciences* 200 (1063) (1950) 523–541.
- [46] H. A. Barnes, J. F. Hutton, K. Walters, *An Introduction to Rheology*, vol. 3, Elsevier, 1989.
- [47] F. Pimenta, M. A. Alves, Stabilization of an open-source finite-volume solver for viscoelastic fluid flows, *Journal of Non-Newtonian Fluid Mechanics* 239 (2017) 85–104.
- [48] F. Pimenta, M. A. Alves, RheoTool: Toolbox to simulate GNF and viscoelastic fluid flows in OpenFOAM, Version

- 5.0, <https://github.com/fppimenta/rheoTool>, 2022.
- [49] OpenFOAM Foundation, OpenFOAM - The Open Source CFD Toolbox, <https://www.openfoam.org/>, 2022.
- [50] M. A. Alves, P. J. Oliveira, F. T. Pinho, A convergent and universally bounded interpolation scheme for the treatment of advection, *International Journal for Numerical Methods in Fluids* 41 (1) (2003) 47–75.
- [51] C. Geuzaine, J. F. Remacle, Gmsh: A 3-D finite element mesh generator with built-in pre- and post-processing facilities, *Int. J. Numer. Meth. Engng.* 79 (2009) 1309 – 1331, <https://gmsh.info/>.
- [52] S. Balay, S. Abhyankar, M. F. Adams, J. Brown, P. Brune, K. Buschelman, L. Dalcin, A. Dener, V. Eijkhout, W. D. Gropp, D. Kaushik, M. G. Knepley, D. A. May, L. C. McInnes, R. T. Mills, T. Munson, K. Rupp, P. Sanan, B. F. Smith, S. Zampini, H. Zhang, H. Zhang, PETSc Web page, <https://www.mcs.anl.gov/petsc>, 2021.
- [53] S. Balay, S. Abhyankar, M. F. Adams, J. Brown, P. Brune, K. Buschelman, L. Dalcin, A. Dener, V. Eijkhout, W. D. Gropp, D. Kaushik, M. G. Knepley, D. A. May, L. C. McInnes, R. T. Mills, T. Munson, K. Rupp, P. Sanan, B. F. Smith, S. Zampini, H. Zhang, H. Zhang, PETSc Users Manual, Tech. Rep. ANL-95/11 - Revision 3.15, Argonne National Laboratory, 2021.
- [54] M. Ajiz, A. Jennings, A robust incomplete Choleski-conjugate gradient algorithm, *International Journal for Numerical Methods in Engineering* 20 (5) (1984) 949–966.
- [55] J. Lee, J. Zhang, C.-C. Lu, Incomplete LU preconditioning for large scale dense complex linear systems from electromagnetic wave scattering problems, *Journal of Computational Physics* 185 (1) (2003) 158–175.
- [56] R. Fattal, R. Kupferman, Constitutive laws for the matrix-logarithm of the conformation tensor, *Journal of Non-Newtonian Fluid Mechanics* 123 (2-3) (2004) 281–285.
- [57] J. Zhou, I. Papautsky, Viscoelastic microfluidics: progress and challenges, *Microsyst. Nanoeng.* 6 (2020) 112.
- [58] M. Alves, P. Oliveira, F. Pinho, Numerical Methods for Viscoelastic Fluid Flows, *Annual Review of Fluid Mechanics* 53 (2021) 509–541.
- [59] M. Kumar, J. S. Guasto, A. M. Ardekani, Lagrangian stretching reveals stress topology in viscoelastic flows, *Proceedings of the National Academy of Sciences* 120 (5) (2023) e2211347120.
- [60] H.-S. Dou, N. Phan-Thien, The flow of an Oldroyd-B fluid past a cylinder in a channel: adaptive viscosity vorticity (DAVSS- ω) formulation, *Journal of Non-Newtonian Fluid Mechanics* 87 (1) (1999) 47–73.
- [61] Y. Fan, R. I. Tanner, N. Phan-Thien, Galerkin/least-square finite-element methods for steady viscoelastic flows, *Journal of Non-Newtonian Fluid Mechanics* 84 (2-3) (1999) 233–256.
- [62] J. Sun, M. Smith, R. Armstrong, R. Brown, Finite element method for viscoelastic flows based on the discrete adaptive viscoelastic stress splitting and the discontinuous Galerkin method: DAVSS-G/DG, *Journal of Non-Newtonian Fluid Mechanics* 86 (3) (1999) 281–307.

- [63] R. P. Bharti, R. P. Chhabra, V. Eswaran, Steady Flow of Power Law Fluids across a Circular Cylinder, *The Canadian Journal of Chemical Engineering* 84 (4) (2006) 406–421.
- [64] S. Claus, T. N. Phillips, Viscoelastic flow around a confined cylinder using spectral/hp element methods, *Journal of Non-Newtonian Fluid Mechanics* 200 (2013) 131–146.